Effects of orientation and strain on the topological characteristics of CdTe/α-Sn quantum wells

G. J. de Coster,[1,2] P. A. Folkes,[1] P. J. Taylor,[1] and O. A. Vail[1]
[1]*US Army Research Laboratory, Adelphi, Maryland 20783, USA*
[2]*Department of Physics, University of Oregon, Eugene, Oregon 97403, USA*

(Received 11 May 2018; published 26 September 2018)

It is known that compressive or tensile planar strain determines the band structure topology of the diamond cubic allotrope of tin (α-Sn) to be either a Dirac semimetal (DSM) or topological insulator (TI), respectively. Using analytical techniques, we show that quantum confinement in negatively strained CdTe/α-Sn quantum wells induces a phase transition from the DSM state to a quasi-three-dimensional TI as α-Sn thickness is decreased. The critical thickness of the transition is found to depend strongly on the orientation of the CdTe, and magnitude of the epitaxial strain, which can be experimentally tuned. This result provides a new rationale for why α-Sn has been observed in a three-dimensional (3D) TI state when pseudomorphically grown on zincblende substrates possessing smaller lattice constants. Additional impacts of strain and orientation on the electronic properties and spin texture of α-Sn are explored. In particular, we examine the impact of orientation on the critical length of the Bernevig-Hughes-Zhang transition from a 2D TI to trivial insulator, as well as on the Rashba spin orbit coupling effects of an external electric field.

DOI: 10.1103/PhysRevB.98.115153

I. INTRODUCTION

The diamond cubic lattice allotrope of tin, known as α-Sn, has long been known to be a zero-gap semiconductor with an inverted band ordering of the Γ_8^+ and Γ_7^- electronic bands due to strong spin-orbit coupling and a large mass-Darwin effect [1,2]. This band inversion prompted several impressive experimental studies in the 1960's and 1970's [3–5], and motivated Abrikosov and Beneslavksii to theoretically study zero-gap semiconductors and Dirac semimetals (DSMs) as early as 1971 [6]. In 2007, Fu and Kane observed that positive epitaxial (tensile in-plane) strain $\epsilon_\parallel > 0$, gaps the conduction and valence bands in α-Sn to make it a three-dimensional (3D) topological insulator (TI) [7], Conversely, for $\epsilon_\parallel < 0$ (compressive in-plane strain), the conduction and valence bands overlap with two Dirac points emerging near the Γ point of the Brillouin zone (BZ) along the k_z axis [5,8], making α-Sn a DSM.[1] Additionally, as the topological band inversion in α-Sn is between the conduction $\Gamma_{8,c}^+$ and subvalence Γ_7^- bands, α-Sn possess a topological surface state (TSS) for all small values of epitaxial strain [9].

Molecular beam epitaxy (MBE) growth of α-Sn on different substrates has yielded seemingly conflicting behaviors. Thin films of α-Sn grown on InSb(001) have been observed to be 3D TIs [10–13]. When grown on InSb(111), α-Sn has been shown to be a DSM [14,15]. On CdTe(111), α-Sn thin films were shown to have a bulk band gap [16]. This variation in observations has been suggested to be the result of different strain or substrate orientation [14], however, in all three cases the α-Sn was negatively strained by the smaller lattice constant of the substrate. In this work we show that the source of the varied experimental results is a quantum confinement induced bulk band gap in the DSM state of α-Sn. The presence of the band-inversion-induced TSS in α-Sn causes the bulk band gap state to experimentally mimic the properties of thin films of 3D TIs subject to quantum confinement effects [17], and the bulk band gap state will henceforth referred to as the quasi-3D TI state [10].

As a case study, we explore the effects of quantum confinement on CdTe(111)/α-Sn and CdTe(001)/α-Sn quantum wells (QWs) using the envelope function approximation (EFA) [18]. We will show that for any $\epsilon_\parallel < 0$ there is a critical thickness of α-Sn L_C, such that an α-Sn layer thicker than L_C will be a DSM. Once the α-Sn layer thickness is less than L_C, it enters a quasi-3D TI phase. Furthermore, due to the strong effective mass anisotropy in α-Sn [3], the values for L_C strongly depend on the substrate orientation. Therefore, there are α-Sn thicknesses for which a CdTe(001)/α-Sn QW would be a DSM while a CdTe(111)/α-Sn QW would be a 3D TI. Finally, L_C is also strongly dependent on $\epsilon_\parallel$, and we will show that L_C drops quickly as $|\epsilon_\parallel|$ is increased. This result was not seen in previous *ab initio* studies [19–22].

The EFA analysis further allows us to identify the critical thicknesses associated with the topological phase transitions between the quasi-3D TI, 2D TI, and trivial insulator phases as was first done for CdTe/HgTe QWs [23,24], and compare these critical lengths for the CdTe(001)/α-Sn and CdTe(111)/α-Sn QWs. As a final point of comparison between the two orientations, we compute the Bernevig-Hughes-Zhang (BHZ) Hamiltonian for the 2D TI phase of CdTe(111)/α-Sn [23]. The (111)-axis threefold rotational symmetry of the diamond lattice gives rise to terms in the BHZ Hamiltonian that are not present in (001)-oriented systems [25], which we show enables the ability to shift the energy of the Dirac point of the helical edge states (HESs) linearly with an applied out-of-plane electric field.

[1]Note that for both negative and positive epitaxial strain, the $Fd\bar{3}m$ symmetry of diamond α-Sn is reduced to a tetragonal $I4_1/amd$ symmetry, for more details see Ref. [8].

The paper is organized as follows. In Sec. II, we will present the (111)-oriented $\boldsymbol{k}\cdot\boldsymbol{p}$ Hamiltonian for QWs that takes into account epitaxial strain, and highlight its contrasts to the (001) $\boldsymbol{k}\cdot\boldsymbol{p}$ Hamiltonian [26]. In Sec. III we demonstrate the quantum confinement-induced transition between the DSM and quasi-3D TI states of CdTe(111)/α-Sn and CdTe(001)/α-Sn, and examine how it depends on strain and orientation. Additionally, the topological phase transitions from the quasi-3D TI to 2D TI, and 2D TI to trivial insulator phases are determined. In Sec. IV we compute the BHZ Hamiltonian for CdTe(111)/α-Sn QWs, and explore the impact of the (111)-axis threefold rotational symmetry on the spin textures and Dirac point of the HES.

II. (111) QUANTUM WELLS $k\cdot p$ MODEL

In order to perform the EFA analysis, we need the 6×6 Kane Hamiltonian acting on the symmetry adapted basis functions for the Γ_7^- and Γ_8^+ bands in the (111) and (001) orientations [26]. We present the (111) case here, the (001) case is well known and can be found in Appendix A. In both cases, the ordered basis of states is given by [27]:

$$\begin{aligned}
\{|1\rangle &= |\Gamma_7^-, +1/2\rangle = |S\rangle|\uparrow\rangle, \quad |2\rangle = |\Gamma_7^-, -1/2\rangle = |S\rangle|\downarrow\rangle\\
|3\rangle &= |\Gamma_8^+, +3/2\rangle = \sqrt{1/2}\,|X+iY\rangle|\uparrow\rangle\\
|4\rangle &= |\Gamma_8^+, +1/2\rangle = \sqrt{1/6}(|X+iY\rangle|\downarrow\rangle - 2|Z\rangle|\uparrow\rangle)\\
|5\rangle &= |\Gamma_8^+, -1/2\rangle = -\sqrt{1/6}(|X-iY\rangle|\uparrow\rangle + 2|Z\rangle|\downarrow\rangle)\\
|6\rangle &= |\Gamma_8^+, -3/2\rangle = -\sqrt{1/2}\,|X-iY\rangle|\downarrow\rangle\}. \qquad (2.1)
\end{aligned}$$

The s-like $|\Gamma_7^- \pm 1/2\rangle$ states are composed of spin $|\uparrow/\downarrow\rangle$ and the spatial $L=0$ basis function $|S\rangle$. The p-like heavy-hole $|\Gamma_8^+ \pm 3/2\rangle$ and light-hole $|\Gamma_8^+ \pm 1/2\rangle$ states are composed of spin with the spatial $L=1$ basis functions $|X\rangle, |Y\rangle, |Z\rangle$, rotated to suit the orientation under consideration. Within Burt-Foreman theory [18,28–30], using the Stravinou-van Dalen Hamiltonian one can derive the (111) oriented QW $\boldsymbol{k}\cdot\boldsymbol{p}$ Hamiltonian [31]:

$$H(\boldsymbol{k}) = \begin{pmatrix} h_{ss} & h_{sp} \\ h_{sp}^\dagger & h_{pp}\end{pmatrix}, \qquad (2.2)$$

with

$$h_{ss} = \begin{pmatrix} E_{\Gamma_7^-}+T & 0 \\ 0 & E_{\Gamma_7^-}+T\end{pmatrix},$$

$$h_{sp} = \begin{pmatrix} -\frac{1}{\sqrt{2}}Pk_+ & \sqrt{\frac{2}{3}}Pk_z & \frac{1}{\sqrt{6}}Pk_- & 0 \\ 0 & -\frac{1}{\sqrt{6}}Pk_+ & \sqrt{\frac{2}{3}}Pk_z & \frac{1}{\sqrt{2}}Pk_-\end{pmatrix},$$

$$h_{pp} = \left(E_{\Gamma_8^+}+U\right)\mathbb{1}_{4\times 4} + \begin{pmatrix} V & -S_- & R & 0 \\ -S_-^\dagger & -V & C & R \\ R^\dagger & C^\dagger & -V & S_+^\dagger \\ 0 & R^\dagger & S_+ & V\end{pmatrix},$$

where P is the momentum matrix element, and

$$k_\parallel^2 = k_x^2 + k_y^2, \quad k_\pm = k_x \pm ik_y, \quad k_z = -i\partial_z,$$
$$\epsilon = \mathrm{tr}\,\tilde{\epsilon} = \epsilon_{xx}+\epsilon_{yy}+\epsilon_{zz},$$

$$\begin{aligned}
T &= \frac{\hbar^2}{2m_e}(\gamma_0 k_\parallel^2 + k_z\gamma_0 k_z) + a'\epsilon,\\
U &= -\frac{\hbar^2}{2m_e}(\gamma_1 k_\parallel^2 + k_z\gamma_1 k_z) - a\epsilon,\\
V &= -\frac{\hbar^2}{2m_e}(\gamma_3 k_\parallel^2 - 2k_z\gamma_3 k_z) - \sqrt{3}d\epsilon_{xy},\\
S_\pm &= -\frac{\hbar^2}{2m_e}\sqrt{3}k_\pm(\{\bar{\gamma}_1, k_z\} + [\kappa, k_z]) + \frac{\hbar^2}{2m_e}\sqrt{\frac{2}{3}}\mu k_\mp^2,\\
R &= -\frac{\hbar^2}{2m_e}\sqrt{\frac{2}{3}}k_+\{k_z, \mu\} + \frac{\hbar^2}{2m_e}\sqrt{3}\bar{\gamma}_2 k_-^2,\\
C &= \frac{\hbar^2}{m_e}k_-[\kappa, k_z].
\end{aligned}$$

Here m_e is the bare electron mass, the coefficients $\gamma_{i=1,2,3}$ are the modified Luttinger parameters, appropriate to the Kane model, and a, a', b, and d are the deformation potentials. For notational brevity we have defined $\mu = (\gamma_2 - \gamma_3)$, $\bar{\gamma}_1 = (2\gamma_2+\gamma_3)/3$, and $\bar{\gamma}_2 = (2\gamma_3+\gamma_2)/3$. The effects of (111) epitaxial strain have been included via the deformation potentials in Eq. (2.2) according to the generalized methods of Pikus and Bir [36,37]. For (111)-oriented crystals under epitaxial strain, the strain tensor $\tilde{\epsilon}$, takes the form:

$$\tilde{\epsilon} = \epsilon_{xx}\delta_{ij} + \epsilon_{xy}(1-\delta_{ij}). \qquad (2.3)$$

For an epitaxial strain $\epsilon_\parallel$ the components of $\tilde{\epsilon}$ are related to the elastic stiffness constants c_{ij}:

$$\epsilon_{xx} = \epsilon_\parallel \frac{4c_{44}}{c_{11}+2c_{12}+4c_{44}} = 0.53\epsilon_\parallel \qquad (2.4a)$$

$$\epsilon_{xy} = -\epsilon_\parallel \frac{c_{11}+2c_{12}}{c_{11}+2c_{12}+4c_{44}} = \epsilon_{xx} - \epsilon_\parallel = -0.47\epsilon_\parallel. \qquad (2.4b)$$

Assuming pseudomorphic growth of α-Sn on CdTe, the epitaxial strain is given by $\epsilon_\parallel = a_l^{ct}/a_l^s - 1 = -0.00126$, with $a_l^{s/ct}$ the lattice constant of α-Sn/CdTe. All Kane parameters and elastic coefficients can be found in Table I.

The parameters for CdTe taken from Novik *et al.* were originally fit so that the momentum matrix element P was equal for CdTe and HgTe [32]. This simplifies the boundary conditions at the interface of the QW [29,38]. To maintain this simplicity in the CdTe/α-Sn QW problem, we shift $P^{ct} \to P^s$, which necessitates modifying the Luttinger parameters $\gamma_{i=0,\ldots,3}$ and κ to leave the effective masses of CdTe energy bands at the Γ point unchanged. Additionally, the Hamiltonian in Eq. (2.2) does not act on the states of the split off Γ_7^- band. In Appendix B we detail how the parameters in Table I are renormalized so that P is the same everywhere, and then modified to account for the coupling between our basis set and the $|\Gamma_7^-\rangle$ states [39].

Before proceeding with calculations, it is useful to observe the key differences between the (111) and (001) Kane Hamiltonians. First, within the V term, the Luttinger parameter γ_3 in the (111) case becomes γ_2 in the (001) case. α-Sn has the property $\gamma_2\gamma_3 < 0$, which results in a large effective mass anisotropy between the (111) and (001) orientations [4]. Additionally, the separate shear deformations d and b modify the Γ_8^+ energy levels in the (111) and (001) orientations, respec-

TABLE I. Table of bare parameters for CdTe/α-Sn QWs. We assume a band offset of $E^{\alpha-\mathrm{Sn}}_{\Gamma_8^+} - E^{\mathrm{CdTe}}_{\Gamma_8^+} = 1.1$ eV [16]. Note $E_p = 2m_e P^2/\hbar^2$, and $\hbar^2/(2m_e) = 3.809982\,\mathrm{eV\,\AA}^2$. The quantity Δ is the spin orbit coupling splitting.

	γ_0	γ_1	γ_2	γ_3	κ	P (eV Å)	E_P (eV)	Δ (eV)	E_g (eV)
α-Sn	1	4.19 [4]	−1.73 [4]	1.64 [4]	−2.18 [4]	9.55 [4]	23.93 [4]	0.80 [4]	−0.413 [4]
CdTe	0.82 [32]	1.47 [32]	−0.28 [32]	0.03 [32]	−1.31 [32]	8.46 [32]	18.8 [32]	0.91 [32]	1.606 [32]
	a (eV)	b (eV)	d (eV)	a' (eV)	c_{11} (10 GPa)	c_{12} (10 GPa)	c_{44} (10 GPa)	a_l (Å)	
α-Sn	7.77 [33]	−2.4 [5]	−4.1 [5]	−14.81 [33,34]	6.90 [34,35]	2.93 [34,35]	3.62 [34,35]	6.4892 [35]	
CdTe	–	–	–	–	5.35 [35]	3.69 [35]	2.02 [35]	6.481 [35]	

tively. For these reasons one can expect significant differences in the quasi-3D TI to DSM crossover lengths between orientations. Next, it is important to note that the $S_\pm$ and R terms in the (111) case possess terms both even and odd in z, whereas in the (001) case, S is only odd and R is only even. These modifications reflect the C_3 rotational symmetry about the z axis of a (111)-oriented diamond lattice. It is the technical reason that certain matrix elements are nonzero in Sec. IV.

III. BAND CROSSINGS

We calculate the evolution of α-Sn's electron band structure as a function of its thickness using the EFA, and determine the crossing points of different bands. We do this by solving the Kane Hamiltonian at $k_x = k_y = 0$ analytically using the standard BHZ-type methods [23,40], and monitor the evolution of the bands' energies to very large QW thicknesses. The plots in Figs. 1(a), 1(b) and 1(c) show the evolution of the various energy levels in the (111)-oriented QWs. Similar plots for the (001) orientation can be found in Appendix C.

Let us define the energies in Fig. 1(a): E($n \geqslant 2$), Hh($n \geqslant 1$), and Lh($n \geqslant 2$) are, respectively, the energies of the bulk conduction, heavy-hole valence, and subvalence bands at the 2D Γ point $k_x = k_y = 0$. The bulk inversion symmetry of the diamond lattice of α-Sn makes all energy levels spin degenerate. In the infinite α-Sn thickness limit, the bottom of the conduction band lies below the top of the valence band at the Γ point, i.e., E2 < Hh1, signaling the DSM phase of α-Sn when $\epsilon_\parallel < 0$.

The E1 and Lh1 bands, respectively, correspond to the symmetric and antisymmetric hybridizations of the topological surface states of 3D α-Sn. As the α-Sn layer decreases in thickness, the bands hybridize more, gapping away from each other. If the α-Sn layer is thin enough, it is effectively a 2D system, and the Dirac surface states of the 3D system become bulk bands of the 2D system. The thickness that corresponds to "thin enough" can be defined as $2l_p$, where l_p is the penetration length of the topological surface states in the infinite thickness limit. For (111)-oriented α-Sn, we determine $l_p = 31.4$ Å, and for the (001) orientation $l_p = 31.7$ Å. These lengths are comparable because they depend strongly on the energy gap $E_{\Gamma_8^+} - E_{\Gamma_7^-}$, which has similar values for both orientations. This is because strain in α-Sn shifts the energy levels $E_{\Gamma_8^+}$ and $E_{\Gamma_7^-}$ according to the T, U, and V terms in Eq. (2.2), but effects only a small relative change in the energy level difference.

The BHZ transition between a 2D trivial and 2D TI state is found at 27 Å in the (111) orientation and 39 Å in the (001) orientation, reflecting the large effective mass anisotropy. This is determined by the crossing of the E1 and Hh1 bands in Fig. 1(b).

The novel feature we focus on is the crossing of the E2 and Hh1 bands at a critical length $L_C = 410$ Å for the (111) orientation, and $L_C = 377$ Å for (001). The (111) crossing can be seen in Fig. 1(c). For thicknesses smaller than L_C the α-Sn layer is a quasi-3D TI, as for all $n \geqslant 2$, E$n \geqslant$ Hh1. The first few bulk electron and heavy-hole energy levels and corresponding k_z momenta for 340 Å thick α-Sn in CdTe(001)/α-Sn QWs are plotted in the bottom right inset of Fig. 2. The positive gap between E2 and Hh1 makes the system bulk insulating, and a Dirac surface state hybridized with the heavy-hole states between L2 and E2 forms between the Γ_7^- band and the Γ_8^+ conduction band [7,11,41].

For thicknesses greater than L_C, the bottom of the conduction band is below the top of the valence band: E2 < Hh1. However, for all thicknesses there will be an energy level EN such that Em > Hh1 when $m \geqslant N$. For thicknesses slightly above the critical length $L \gtrsim L_C$, one can see from Fig. 1(c) that E(2, 3) > Hh1. In the infinite α-Sn thickness limit, for $\epsilon_\parallel < 0$, CdTe(001)/α-Sn and CdTe(111)/α-Sn QWs are DSMs with Dirac points along the k_z axis. Exceeding L_C enters the DSM phase, with strongly quantized momenta. The first few energy levels and k_z momenta for 430 Å thick α-Sn in CdTe(001)/α-Sn QWs are plotted in the top left inset of Fig. 2.

Within the calculation we can artificially tune the value of $\epsilon_\parallel$ due to CdTe, while in experiment this could be achieved with pressure. One can now interpret L_C as a function of $\epsilon_\parallel$. $L_C(\epsilon_\parallel)$ is plotted for small strains in the (111) and (001) orientations in Fig. 2. We see that the (111) orientation always possesses a greater L_C than the (001) orientation. Therefore there are α-Sn thicknesses for which CdTe(111)/α-Sn behaves as a TI while CdTe(001)/α-Sn behaves as a DSM. Observe the limiting behavior of $L_C(\epsilon_\parallel)$:

$$\lim_{\epsilon_\parallel \to 0} L_C(\epsilon_\parallel) \to \infty, \tag{3.1a}$$

$$\lim_{\epsilon_\parallel \to -\infty} L_C(\epsilon_\parallel) \to 0. \tag{3.1b}$$

At 0 strain, infinitely thick α-Sn is a zero-gap semiconductor, so quantum confinement makes it a quasi-3D TI with vanishing bulk gap [10]. At infinite strain, the conduction band is always below the valence band, meaning the system is semimetallic for all α-Sn thicknesses. One should note the method of including strain in $\boldsymbol{k}\cdot\boldsymbol{p}$-theory by Pikus and Bir only applies for perturbative strains [36]. When $|\epsilon_\parallel| \gg 1\%$ the method breaks down, as the crystal lattice will generally assume a different structure.

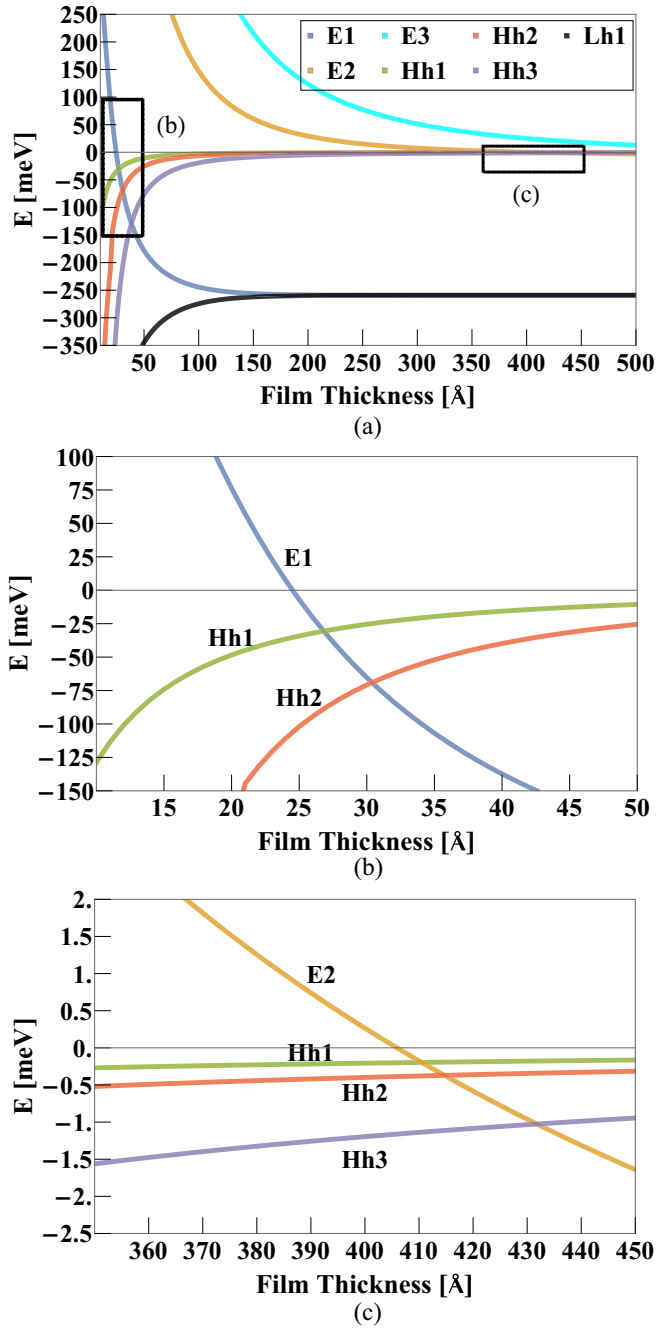

FIG. 1. (a) Plots of the evolution of energy band minima/maxima due to quantum confinement in CdTe(111)/α-Sn QWs as a function of α-Sn thickness. Energies are measured relative to the valence band maximum in the infinite thickness limit $E_{\Gamma_8^+} - a\epsilon - \sqrt{3}d\epsilon_{xy}$. The epitaxial strain on α-Sn due to CdTe is $\epsilon_\parallel = -0.126\%$. The boxes labeled (b) and (c) are blown up in the following figures. (b) The crossover from the 2D trivial insulator state to the 2D TI state is at approximately 27 Å . (c) The crossover from the quasi-3D TI state to the 3D DSM state is at approximately 411 Å.

For an experimental reference, we compare the calculated bulk band gap of $E_g = \mathrm{E2} - \mathrm{Hh1}$ to data obtained by HREEL measurements taken by Tatakani and Chung of α-Sn thin films on CdTe(111) [16]. It is important to note that the inversion symmetry of the QW problem vastly simplifies the analysis compared to the thin film case, in which the Schrödinger equation for the α-Sn electrons and holes has different boundary conditions at the top and bottom of the film. Thus in a QW, the eigenstates are purely odd/even about the well center, whereas in a thin film they are not. This makes the analytical solution in the thin film problem fundamentally harder [42]. However, by accounting for the coupling between the Γ_7^- and Γ_8^+ bands using Löwdin perturbation theory, one can arrive at a decoupled Schrödinger equation for the electrons and holes. By modeling the thin film as a half-infinite well, i.e., vacuum boundary conditions on the top and CdTe(111) boundary conditions on the bottom, one can solve the Schrödinger equation to obtain the energy levels $\mathrm{E}(n \geqslant 2)$ and $\mathrm{Hh}(n \geqslant 1)$ (see Appendix D). The calculated E_g matches the experimental data well, as seen in Fig. 3.

The failing of the half-infinite well model is that by eliminating the explicit coupling between inverted bands, it is incapable of revealing information about the Dirac surface states E1 and L1. We find that the thin film calculation for E_g deviates from the QW derived E_g for small thicknesses, but that they approach each other for large thicknesses. The half-infinite well model yields $L_C = 417$ Å for CdTe(111)/α-Sn thin films, which is very close to the L_C for QWs.

IV. MODIFIED BHZ HAMILTONIAN AND SPIN TEXTURES

A (111)-oriented diamond lattice possesses threefold rotational symmetry C_3, about the z axis, which is not present in the (001) case. According to the method of invariants [25,30], C_3 symmetry should generate terms unique to the (111) orientation BHZ Hamiltonian for the 2D TI phase of the CdTe(111)/α-Sn QW. In this section we calculate the BHZ Hamiltonian for 29 Å thick α-Sn, and explore the impact of the C_3 terms on the helical edge states of the 2D TI phase.

The BHZ Hamiltonian corresponds to an effective 2D Hamiltonian for the ordered basis of $\{|\mathrm{E1}+\rangle, |\mathrm{Hh1}+\rangle, |\mathrm{E1}-\rangle, |\mathrm{Hh1}-\rangle\}$, and is obtained by projecting the Kane $\boldsymbol{k}\cdot\boldsymbol{p}$ Hamiltonian onto them in the usual way [23,25]. Using Löwdin perturbation theory (PT), we account for coupling to the $\{|\mathrm{L1}\pm\rangle, |\mathrm{Hh2}\pm\rangle, |\mathrm{Hh3}\pm\rangle\}$ bands. Defining

$$\epsilon_0(\boldsymbol{k}) = C - Dk^2, \quad \mathcal{M}(k) = M - Bk^2, \tag{4.1}$$

we find the C_3 symmetry modified BHZ Hamiltonian:

$$H_0(\boldsymbol{k}) = \epsilon_0(\boldsymbol{k}) + \begin{pmatrix} \mathcal{M}(k) & A_1 k_- & 0 & A_2 k_- \\ A_1 k_+ & -\mathcal{M}(k) & A_2 k_- & 0 \\ 0 & A_2 k_+ & \mathcal{M}(k) & -A_1 k_+ \\ A_2 k_+ & 0 & -A_1 k_- & -\mathcal{M}(k) \end{pmatrix}$$
$$= \epsilon_0(\boldsymbol{k}) + \mathcal{M}(k)\sigma_0 \otimes \tau_z + k_x(A_1\sigma_z + A_2\sigma_x) \otimes \tau_x + k_y(A_1\sigma_0 \otimes \tau_y + A_2\sigma_y \otimes \tau_x), \tag{4.2}$$

and for comparison, we define the standard form of the (001) BHZ Hamiltonian:

$$H_1(\boldsymbol{k}) = \epsilon_0(\boldsymbol{k}) + \begin{pmatrix} \mathcal{M}(k) & \bar{A}k_+ & 0 & 0 \\ \bar{A}k_- & -\mathcal{M}(k) & 0 & 0 \\ 0 & 0 & \mathcal{M}(k) & -\bar{A}k_- \\ 0 & 0 & -\bar{A}k_+ & -\mathcal{M}(k) \end{pmatrix}$$
$$= \epsilon_0(\boldsymbol{k}) + \mathcal{M}(k)\sigma_0 \otimes \tau_z + k_x\bar{A}(\sigma_z \otimes \tau_x) - k_y\bar{A}(\sigma_0 \otimes \tau_y), \tag{4.3}$$

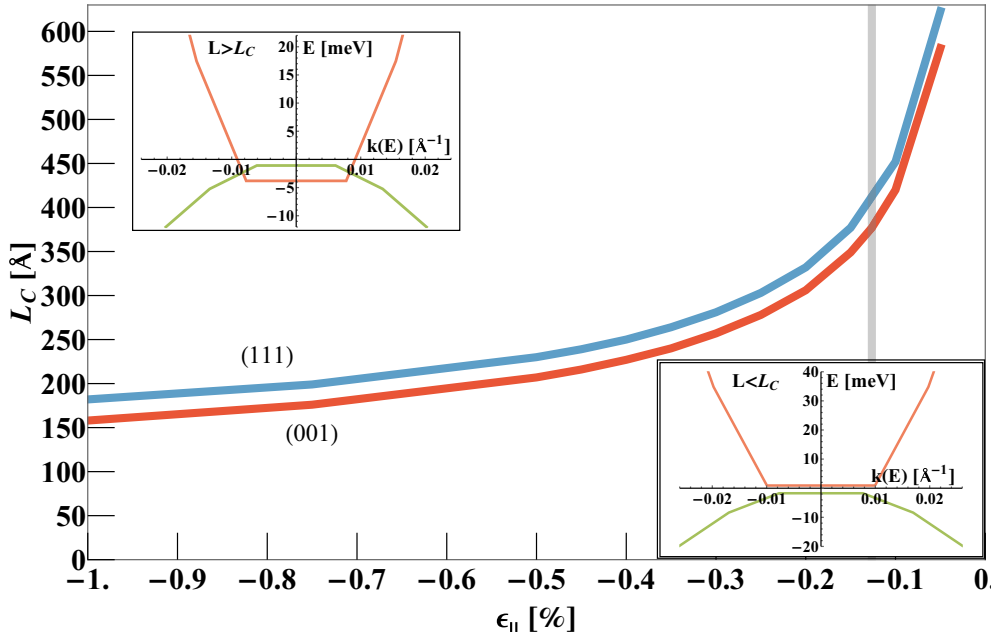

FIG. 2. The epitaxial strain dependence of the critical thickness L_C, of α-Sn(111) (blue) and α-Sn(001) (red) QWs. The vertical gray line denotes $\epsilon_{\parallel} = -0.126\%$, the epitaxial strain of α-Sn grown on CdTe. The insets show sample energy spectra in the (001) direction of the conduction (red) and valence (green) bands for (001)-oriented wells in the TI phase ($L = 340$ Å) and the DSM phase ($L = 430$ Å) for (001) α-Sn on CdTe QWs.

where $\bar{A} = \sqrt{A_1^2 + A_2^2}$. $\sigma_{i=0\ldots3}$ and $\tau_{i=1\ldots3}$ are the usual Pauli matrices acting on spin and electron/heavy-hole degrees of freedom, respectively.

Computing the characteristic polynomials of H_0 and H_1, we find $\det(H_0 - E\mathbb{1}) = \det(H_1 - E\mathbb{1})$. Therefore there exists a unitary transformation W such that $WH_0W^\dagger = H_1$. This equivalence reflects the fact that H_0 and H_1 are derived from different symmetry adapted $\boldsymbol{k}\cdot\boldsymbol{p}$ Hamiltonians of the same system. Technically, the reason A_2 appears in the off-block-diagonal entries in H_0 is because the $S_\pm$ and R terms in the (111) Kane Hamiltonian in Eq. (2.2) lack z parity. That is, they are neither odd nor even functions in z, as mentioned in Sec. II.

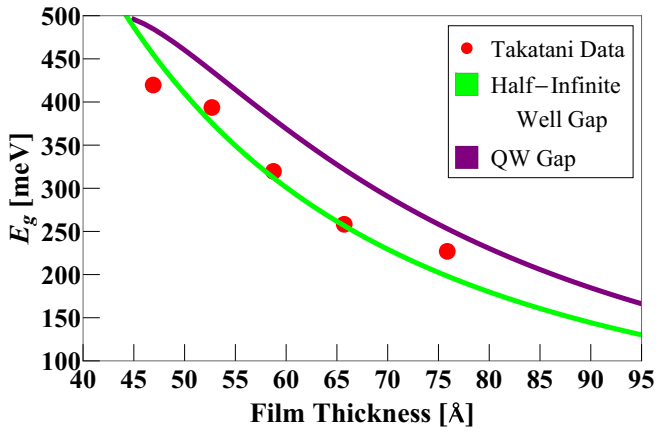

FIG. 3. Comparison of the thin film band gap E_g = E2-Hh1 data and model obtained by Tatakani and Chung for α-Sn grown on CdTe(111) to QW based calculations [16]. The QW energy gap only slightly deviates from the thin film case, as expected. In Appendix D we discuss the half-infinite well gap model used for thin film energy levels.

By applying an electric field $\mathcal{E}_z$ to the QW, one breaks the inversion symmetry across the α-Sn layer, which results in Rashba spin orbit coupling (RSOC) terms in the BHZ Hamiltonian. As a first approximation, the effects of an electric field are included by adding a spatially dependent potential $V(z) = e\mathcal{E}_z z$, to the Kane Hamiltonian. Repeating the Löwdin PT procedure outlined above on $V(z)$ produces the following Rashba Hamiltonian:

$$H_R(\boldsymbol{k}) = \begin{pmatrix} 0 & iS_1k_+^2 & -iR_0k_+ & iS_0k_+^2 \\ -iS_1k_-^2 & 0 & -iS_0k_+^2 & 0 \\ iR_0k_- & iS_0k_-^2 & 0 & -iS_1k_-^2 \\ -iS_0k_-^2 & 0 & iS_1k_+^2 & 0 \end{pmatrix}. \tag{4.4}$$

We have kept only terms up to $\mathcal{O}(k^2)$ and $\mathcal{O}(\mathcal{E}_z)$, and S_0, S_1, and R_0 are all real coefficients that are linearly proportional to $e\mathcal{E}_z$. The S_1 term is allowed by the C_3 symmetry of the (111) orientation, and does not exist in the (001) case. The lack of parity in the R and $S_\pm$ terms in the Kane Hamiltonian make S_0 and S_1 appear at the same order of Löwdin PT as R_0. This means S_0 and S_1 should be treated on the same footing as R_0 in any perturbative calculations.

By calculating the characteristic polynomials of the BHZ Hamiltonians including RSOC, one can show for any renormalization of RSOC parameters

$$\det(H_0 + H_R - E\mathbb{1}) \neq \det(H_1 + H_R' - E\mathbb{1}), \tag{4.5}$$

where H_R' is the (001) Rashba Hamiltonian. This means the (111) and (001) Hamiltonians including RSOC are not equivalent to each other. This reflects the fact that an electric

TABLE II. Parameter values of $H_0(\boldsymbol{k}) + H_R(\boldsymbol{k})$ for a 29 Å thick α-Sn layer.

M (eV)	-1.42×10^{-3}
B (eV nm^2)	-0.640
C (eV)	0.185
D (eV nm^2)	-0.420
A_1 (eV nm)	-0.545
A_2 (eV nm)	5.98×10^{-2}
$R_0/e\mathcal{E}_z$ (nm^2)	2.11
$S_0/e\mathcal{E}_z$ (nm^3)	-0.892
$S_1/e\mathcal{E}_z$ (nm^3)	1.02

field breaks the rotational equivalence of the (001) and (111) orientations.

For this reason one has to study the (111) RSOC Hamiltonian on its own and determine how the effects of a perpendicular electric field on a (111)-oriented QW differ from a (001)-oriented QW. Using the calculated parameters for a 29 Å thick α-Sn layer in Table II, we investigate the spin textures of the HES of the 2D TI phase of CdTe(111)/α-Sn QWs.

A. Spin polarization of edge states

In this section, we project H_0 onto the traditional solutions for the HES, in order to determine their bare spin orientation. For a semi-infinite system in the $x > 0$ plane, the edge state solutions $\psi_{\uparrow/\downarrow}(x)$ to $H_0(-i\partial_x, k_y = 0)$ with $A_2 = 0$ are given in Appendix E 1 following Ortiz *et al.* [43]. Here spin-up/spin-down is with respect to the z direction of the (111) α-Sn. Defining

$$\mathcal{H}'_{ij} = \int dx\ \psi_i^\dagger(x) H_0(-i\partial_x, k_y)\psi_j(x), \tag{4.6}$$

we obtain the bare edge state Hamiltonian $\mathcal{H}$ with right/left mover state energies $E_{R/L}(k_y)$ [44]:

$$\mathcal{H}' = C - \frac{MD}{B} + k_y \frac{\sqrt{B_+B_-}}{|B|}\begin{pmatrix} |A_1| & -|A_2| \\ -|A_2| & -|A_1| \end{pmatrix}, \tag{4.7}$$

$$E_{R/L}(k_y) = C - \frac{MD}{B} \pm k_y \bar{A}\frac{\sqrt{B_+B_-}}{|B|}, \tag{4.8}$$

where $B_\pm = B \pm D$. We have thus obtained the bare Dirac edge state dispersion, it is plotted in Fig. 4 along with several bulk bands. The right/left moving edge states thus have spin polarization:

$$\langle \boldsymbol{S}_{R/L}\rangle = \pm\frac{1}{\sqrt{A_1^2 + A_2^2}}(|A_2|, 0, -|A_1|)^T. \tag{4.9}$$

This shows that for the (111) orientation, the threefold rotational symmetry enforces an in-plane component to the edge states' spin polarization.

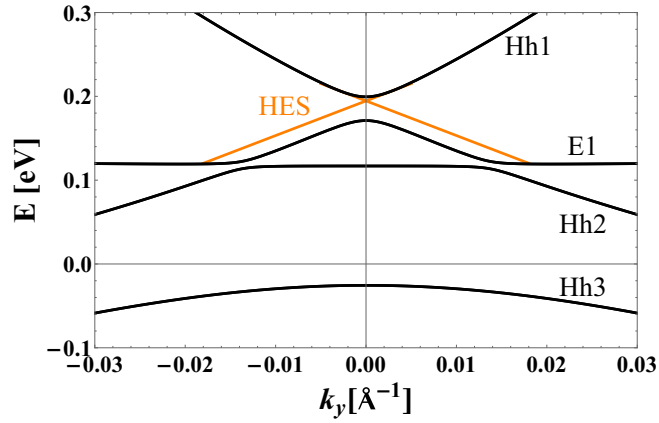

FIG. 4. Plot of calculated Dirac HES dispersion (orange) and bulk bands (black) of a 29 Å thick α-Sn layer in a CdTe/α-Sn QW. The band L1 is far below Hh3 and not shown.

B. Spin texture of edge states

Now let us consider the following transformation that is nontrivial in spin space:

$$W = m_{A_2} \otimes \begin{pmatrix} -1 & 0 \\ 0 & A_1/\bar{A} \end{pmatrix} + n_{A_2} \otimes \begin{pmatrix} 0 & 0 \\ 0 & -A_2/\bar{A} \end{pmatrix}$$

$$(m_{A_2}, n_{A_2}) = \begin{cases} (\sigma_x, \sigma_z) & \text{for } A_2 > 0 \\ (i\sigma_y, \sigma_0) & \text{for } A_2 < 0 \end{cases}. \tag{4.10}$$

The action of W is

$$W H_0(\boldsymbol{k}) W^\dagger = H_1(\boldsymbol{k}) \tag{4.11}$$

$$W H_R(\boldsymbol{k}) W^\dagger = \begin{pmatrix} 0 & i\tilde{S}_1 k_-^2 & -i\tilde{R}_0 k_- & i\tilde{S}_0 k_-^2 \\ -i\tilde{S}_1 k_+^2 & 0 & -i\tilde{S}_0 k_-^2 & 0 \\ i\tilde{R}_0 k_+ & i\tilde{S}_0 k_+^2 & 0 & -i\tilde{S}_1 k_+^2 \\ -i\tilde{S}_0 k_+^2 & 0 & i\tilde{S}_1 k_-^2 & 0 \end{pmatrix}$$

$$\equiv \tilde{H}_R(\boldsymbol{k}). \tag{4.12}$$

We define the renormalized coefficients:

$$\tilde{R}_0 = R_0 \operatorname{sgn} A_2 \tag{4.13a}$$

$$\tilde{S}_0 = \frac{A_1 S_0 - A_2 S_1}{\bar{A}} \operatorname{sgn} A_2 \tag{4.13b}$$

$$\tilde{S}_1 = \frac{A_2 S_0 + A_1 S_1}{\bar{A}}. \tag{4.13c}$$

Assuming a semi-infinite material for $x > 0$, we solve $H_0(-i\partial_x, k_y)$ explicitly for the edge states $\phi_\pm(k_y)$ in Appendix E 2. We then project $[H_0 + \tilde{H}_R](-i\partial_x, k_y)$ onto the HES to obtain the effective RSOC edge Hamiltonian $\mathcal{H}$, from which the spin textures of the HES are computed. Defining the RSOC edge Hamiltonian:

$$\mathcal{H}_{ij} = \int dx\ \psi_i^\dagger(x)[H_0 + \tilde{H}_R](-i\partial_x, k_y)\psi_j(x), \tag{4.14}$$

we obtain:

$$\mathcal{H} = E_D + k_y \begin{pmatrix} v & \alpha_{k_y} \\ \alpha_{k_y} & -v \end{pmatrix}. \tag{4.15}$$

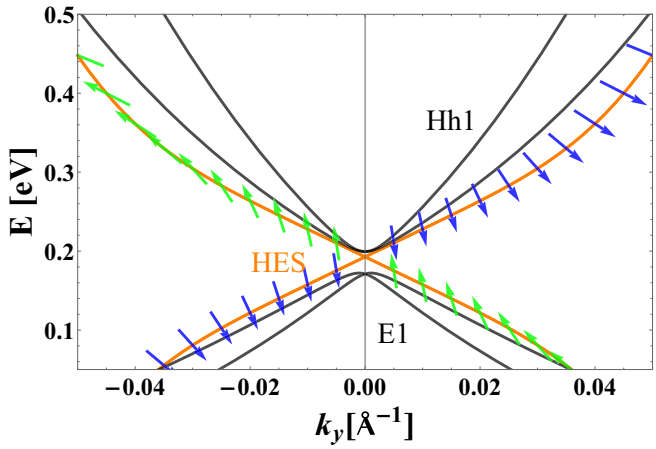

FIG. 5. Spin textures of the HES band (orange) imposed on the edge state for an applied field of strength $\mathcal{E}_z = 0.01$ V Å $^{-1}$, with blue (green) arrows corresponding to right (left) moving states. An up or right arrow, respectively, corresponds to a fully $+S_z$ or $+S_x$ polarized spin. Bulk bands with RSOC taken into account are also plotted (black).

The Dirac point E_D, and Fermi velocity v, now depend on the inversion breaking electric field through $\tilde{S}_1$:

$$E_D = C - \frac{MD}{B} - \frac{M\sqrt{B^2 - D^2}}{B^2}\tilde{S}_1 \tag{4.16}$$

$$v = \left(\sqrt{B_+ B_-} + \frac{\tilde{S}_1 D}{B}\right)\frac{\bar{A}}{B}. \tag{4.17}$$

The spin texture term α_{k_y} is given explicitly in Appendix E 2. To $\mathcal{O}(k^2)$ it is

$$\alpha_{k_y} = \tilde{R}_0 \frac{(B-D)^2}{2B^2}\left(1 - a k_y^2\right) + \mathcal{O}\left(k_y^4\right) \tag{4.18}$$

$$a = D^2 \frac{\bar{A}^2 B + 2(B^2 - D^2)M}{2BM^2(B^2 - D^2)}. \tag{4.19}$$

The edge state Hamiltonian is trivial to diagonalize, and one can compute the momentum dependent spin polarization of the HES:

$$\langle \boldsymbol{S}_\pm \rangle = \pm \frac{1}{\sqrt{v^2 + \alpha_{k_y}^2}}\left(\alpha_{k_y}, 0, v\right)^T. \tag{4.20}$$

From the above result we see that when $\mathcal{E}_z = 0$, we have $\langle \boldsymbol{S}_\pm \rangle = \pm\hat{z}$. Thus, the calculation of $\langle \boldsymbol{S}_\pm \rangle$ in the $\phi_\pm$ basis is equivalent to rotating $\langle \boldsymbol{S}_{R/L} \rangle$ in Eq. (4.9) to the $\pm\hat{z}$ directions. For $\mathcal{E}_z = 0$, it is easy to see there exists a unitary transformation V such that $V\mathcal{H}V^\dagger = \mathcal{H}'$. Then for $\mathcal{E}_z \neq 0$, the spin polarization of the eigenstates of $V\mathcal{H}V^\dagger$ yields the true spin texture, in which the z axis is the (111) direction of α-Sn. The HES with this spin texture, and bulk bands with RSOC are plotted in Fig. 5.

V. CONCLUSION AND OUTLOOK

We have demonstrated that quantum confinement induces a thickness-dependent transition between a band overlap DSM phase and bulk band gap quasi-3D TI phase in CdTe/α-Sn QWs and thin films. The critical thickness of this transition L_C, was found to depend strongly on the orientation and strain of α-Sn in the QW system. We also found that the BHZ transition of the 2D TI to trivial insulator is strongly affected by orientation.

Our findings phenomenologically resolve the ambiguity in the literature that thin films of α-Sn grown on zincblende substrates are found in different 3D topological states despite $\epsilon_\parallel < 0$ in α-Sn for all cases [12,14,16]. While repeating these calculations for InSb/α-Sn QWs would allow for comparison to modern experimental results, this would require knowledge of the valence band offset between InSb and α-Sn. Additionally, we have seen that a strong strain pushes L_C to small thicknesses of α-Sn, which could be accessible with density functional theory (DFT) based calculations. This would provide an alternative theoretical method of investigating the quasi-3D TI to DSM transition. Recently, a quantum-confinement-induced band gap in the DSM Cd_3As_2 was observed [45], indicating the DSM to quasi-3D TI transition may be common. The thickness at which the gap opens in Cd_3As_2 may be identifiable in the manner we have presented.

We have also found that orientation affects the 2D TI phase of CdTe/α-Sn QWs in a striking manner. By calculating the RSOC BHZ Hamiltonian for a 29 Å thick layer of α-Sn in CdTe(111)/α-Sn, we showed that an out-of-plane electric field shifts the energy of the HES Dirac point linearly as a function of field strength, which is not the case for the (001) orientation. Moreover, we found that the threefold rotational symmetry terms in the modified BHZ Hamiltonian enforce an in-plane component to the bare spin polarization of the HES.

One open question following our study is the impact of the CdTe(111) surface on our results. The CdTe(111) surface is either Cd or Te terminated (A and B termination, respectively), and thus polar. In turn, there is an electrostatic potential $V(z)$ about the CdTe/α-Sn interface that has not been accounted for in the current $\boldsymbol{k}\cdot\boldsymbol{p}$ treatment of the QW states. Assuming a linear potential for small distances from the interface $V(z) \sim z$, then to first order in perturbation theory it would naturally play a role in the spin textures of the edge states in Sec. IV. A complicated $V(z)$ could also modify the energy levels En and Hhn in Sec. III, altering the values of the critical thicknesses for the (111) orientation. *Ab initio* techniques developed to determine the surface potential of CdTe(110)/Sn interfaces could potentially determine $V(z)$ for different CdTe(111) terminations [2]. We emphasize that Te-terminated CdTe(111)B is the more experimentally relevant surface to consider. MBE growth of α-Sn on CdTe(111)A is generally observed to result in films that have rougher surfaces than those grown on CdTe(111)B [46]. On CdTe(111)B, covalent bonding between Sn and surface Te atoms is energetically preferred over the case of CdTe(111)A where the Sn and surface Cd atoms support no covalent compound; only metallic bonding between Sn and Cd is obtained. Covalent bonding facilitates incorporation of the adsorbed Sn atoms on the CdTe(111)B surface into the growing crystal structure, leading to less roughness in α-Sn compared to growth on CdTe(111)A.

Our results indicate great promise for experimental investigations of topological phases in MBE-grown CdTe/α-Sn QWs. In an effort to realize these theoretical calculations experimentally, our group has developed a reliable MBE growth recipe of α-Sn on CdTe based on the methods of Farrow *et al.* [47] as evidenced by Raman spectroscopy and x-ray diffraction characterization [46]. By growing and characterizing films of thicknesses on either side of L_C it should be possible to demonstrate the quantum confinement transition between the DSM and quasi-3D TI states.

ACKNOWLEDGMENTS

We would like to thank Dr. T. Bahder for valuable discussions. This research was partially supported by a Laboratory University Collaborative Initiative award provided by the Basic Research Office in the Office of the Under Secretary of Defense for Research and Engineering.

APPENDIX A: (001) KANE HAMILTONIAN

We present the 6×6 Kane model for (001)-oriented QWs:

$$H_{001}(\boldsymbol{k}) = \begin{pmatrix} E_{\Gamma_7^-} + T & 0 & -\frac{1}{\sqrt{2}}Pk_+ & \sqrt{\frac{2}{3}}Pk_z & \frac{1}{\sqrt{6}}Pk_- & 0 \\ 0 & E_{\Gamma_7^-} + T & 0 & -\frac{1}{\sqrt{6}}Pk_+ & \sqrt{\frac{2}{3}}Pk_z & \frac{1}{\sqrt{2}}Pk_- \\ -\frac{1}{\sqrt{2}}Pk_- & 0 & E_{\Gamma_8^+} + U + V & -S_- & R & 0 \\ \sqrt{\frac{2}{3}}Pk_z & -\frac{1}{\sqrt{6}}Pk_- & -S_-^\dagger & E_{\Gamma_8^+} + U - V & C & R \\ \frac{1}{\sqrt{6}}Pk_+ & \sqrt{\frac{2}{3}}Pk_z & R^\dagger & C^\dagger & E_{\Gamma_8^+} + U - V & S_+^\dagger \\ 0 & \frac{1}{\sqrt{2}}Pk_+ & 0 & R^\dagger & S_+ & E_{\Gamma_8^+} + U + V \end{pmatrix}, \tag{A1}$$

where

$$T = \frac{\hbar^2}{2m_e}(\gamma_0 k_\parallel^2 + k_z\gamma_0 k_z) + a'\epsilon, \quad U = -\frac{\hbar^2}{2m_e}(\gamma_1 k_\parallel^2 + k_z\gamma_1 k_z) - a\epsilon, \quad V = -\frac{\hbar^2}{2m_e}(\gamma_2 k_\parallel^2 - 2k_z\gamma_2 k_z) + b(\epsilon_{xx} - \epsilon_{zz}),$$

$$S_\pm = -\frac{\hbar^2}{2m_e}\sqrt{3}k_\pm(\{\gamma_3, k_z\} + [\kappa, k_z]), \quad R = -\frac{\hbar^2}{2m_e}\sqrt{3}(\mu k_+^2 - \bar{\gamma}k_-^2), \quad C = \frac{\hbar^2}{m_e}k_-[\kappa, k_z].$$

Here we have used the notation of Novik *et al.* [32] where $\mu = (\gamma_3 - \gamma_2)/2$, $\bar{\gamma} = (\gamma_3 + \gamma_2)/2$. For (001) epitaxial strain $\epsilon_\parallel$, we have $\epsilon_{xx} = \epsilon_{yy} = \epsilon_\parallel$ and $\epsilon_{zz} = -2c_{12}\epsilon_\parallel/c_{11} = -0.85\epsilon_\parallel$.

APPENDIX B: FORMULA FOR HAMILTONIAN MODIFICATION

P and $\gamma_{i=0,\ldots,3}$ are fitting parameters that determine the effective masses of energy bands at the Γ point. They can be mutually renormalized in a manner that accounts for the coupling between bands, so that effective masses are left unchanged [29,30,38]. We choose to make P^{ct} equal to P^s, resulting in the renormalizations:

$$\gamma_0 = \gamma_0^{\text{old}} + \frac{E_P^{ct} - E_P^s}{E_g^{ct}} \frac{E_g^{ct} + \frac{2}{3}\Delta^{ct}}{E_g^{ct} + \Delta^{ct}}, \tag{B1a}$$

$$\gamma_1 = \gamma_1^{\text{old}} + \frac{E_P^{ct} - E_P^s}{3E_g^{ct}}, \tag{B1b}$$

$$(\gamma_2, \gamma_3, \kappa) = \left(\gamma_2^{\text{old}}, \gamma_3^{\text{old}}, \kappa^{\text{old}}\right) + \frac{E_P^{ct} - E_P^s}{6E_g^{ct}}. \tag{B1c}$$

Finally, the 6×6 Hamiltonian does not act on the split off band Γ_7^+. To account for the momentum matrix coupling between the Γ_7^+ and Γ_7^- band [39], we must further renormalize γ_0^{ct} according to Löwdin perturbation theory.

$$\gamma_0 \to \gamma_0 + \frac{E_P}{3(\Delta + E_g)}. \tag{B2}$$

The effects of Γ_8^+-Γ_7^+ coupling is ignored as it only impacts $\mathcal{O}(k^4)$ terms [30].

APPENDIX C: (001) ENERGY LEVEL PLOTS

We present in Fig. 6 the EFA determined energy level plots for CdTe(001)/α-Sn QWs.

APPENDIX D: THIN FILM BAND GAP

A very good fit to Tatakani and Chung's band gap data is obtained by treating the problem as a 1D half-infinite quantum well for the light and heavy holes in α-Sn and CdTe [16]. The allowed light-hole ϵ_{lh}, and heavy-hole ϵ_{hh}, energies of the Schrödinger equation in this case are given by:

$$-\cot\left(\frac{2m_{lh}L^2(\epsilon_{lh} - \epsilon_o)}{\hbar^2}\right)^{1/2} = \left[\frac{V - (\epsilon_{lh} - \epsilon_o)}{\epsilon_{lh} - \epsilon_o}\right]^{1/2}, \tag{D1}$$

$$\cot\left(\frac{2m_{hh}L^2(\epsilon_{hh} + \epsilon_o)}{\hbar^2}\right)^{1/2} = \left[-\frac{V + (\epsilon_{hh} + \epsilon_o)}{\epsilon_{hh} + \epsilon_o}\right]^{1/2}, \tag{D2}$$

where $2\epsilon_o = 0.0084$ eV is the strain-induced energy gap of the heavy-/light-hole bands, and $m_{lh} = 0.028m_e$ and $m_{hh} = 0.195m_e$ are the (111) effective mass of the light and heavy holes in α-Sn, respectively. The bulk band gap is then the difference of the light-hole and heavy-hole energies $E_g = \epsilon_{lh} - \epsilon_{hh}$. L is the well thickness, V is the height of the well,

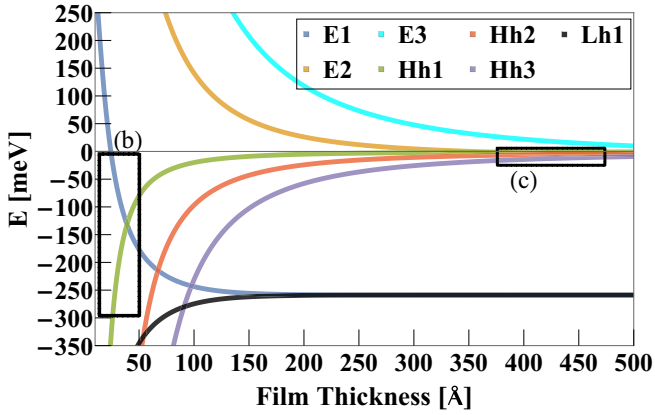

(a)

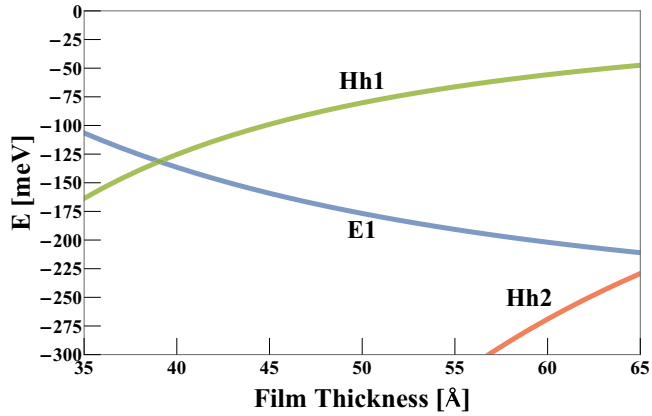

(b)

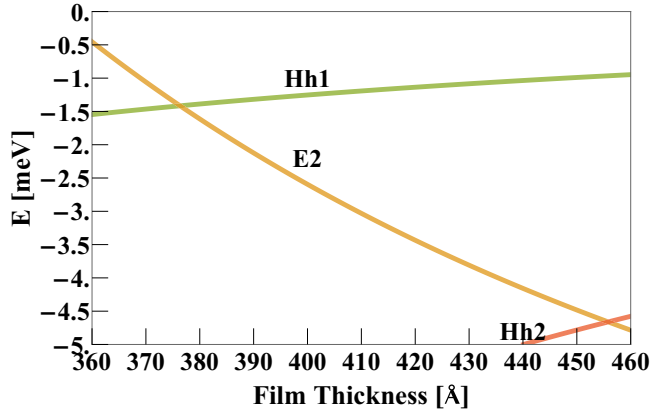

(c)

FIG. 6. (a) Plots of the evolution of energy band minima/maxima due to quantum confinement in CdTe(001)/α-Sn QWs as a function of α-Sn thickness. Energies are measured relative to the valence band maximum in the infinite thickness limit $E_{\Gamma_8^+} - a\epsilon + b(\epsilon_{xx} - \epsilon_{zz})$. The epitaxial strain on α-Sn due to CdTe is $\epsilon_\parallel = -0.126\%$. The boxes labeled (b) and (c) are blown up in the following figures. (b) The crossover from the 2D trivial insulator state to the 2D TI state is at approximately 39 Å. (c) The crossover from the quasi-3D TI state to the 3D DSM state is at approximately 377 Å.

which corresponds to the band offset:

$$V = E^{\alpha\text{-Sn}}_{\Gamma_8^+} - E^{\text{CdTe}}_{\Gamma_8^+} = 1.1 \text{ eV}. \tag{D3}$$

APPENDIX E: FORMULA FOR SPIN TEXTURES

1. Bare spin orientation material

According to Ortiz *et al.* the edge state solutions $\psi_{\uparrow/\downarrow}(x)$ to $H_0(-i\partial_x, k_y = 0)$ with $A_2 = 0$ for the semi-infinite $x > 0$ plane are given by [43]:

$$\psi_\uparrow(x) = \mathcal{N} g(x)\left(-i \text{ sgn } A_1, \frac{\sqrt{B_+B_-}}{B_-}, 0, 0\right)^T, \tag{E1a}$$

$$\psi_\downarrow(x) = \mathcal{N} g(x)\left(0, 0, i \text{ sgn } A_1, \frac{\sqrt{B_+B_-}}{B_-}\right)^T, \tag{E1b}$$

$$g(x) = \sqrt{\frac{2\lambda_1\lambda_2(\lambda_1+\lambda_2)}{(\lambda_1-\lambda_2)^2}}(e^{-\lambda_1 x} - e^{-\lambda_2 x}), \tag{E1c}$$

$$\lambda_{1,2} = \frac{1}{\sqrt{B_-B_+}}\left(\frac{|A_1|}{2} \pm \sqrt{\frac{A_1^2}{4} - \frac{M}{B}B_+B_-}\right), \tag{E1d}$$

$$B\pm = B \pm D, \quad \mathcal{N} = \sqrt{B_-/(2B)}. \tag{E1e}$$

2. Spin texture material

Following once more the work of Ortiz *et al.* the edge eigenstates of the Hamiltonian $H_0(-i\partial_x, k_y)$ for the half-plane $x > 0$ are given by:

$$\phi_\pm(x, k_y) = f(x, \pm k_y)\varphi_\pm, \tag{E2}$$

with energies

$$E_\pm = C - \frac{MD}{B} \pm \sqrt{B_+B_-}\frac{\bar{A}}{B}k_y. \tag{E3}$$

We have defined the following vectors and functions:

$$\varphi_+ = \mathcal{N}\left(-i, \frac{\sqrt{B_+B_-}}{B_-}, 0, 0\right)^T, \tag{E4a}$$

$$\varphi_- = \mathcal{N}\left(0, 0, i, \frac{\sqrt{B_+B_-}}{B_-}\right)^T, \tag{E4b}$$

$$f(x, k_y) = \sqrt{\frac{2\lambda_1\lambda_2(\lambda_1+\lambda_2)}{(\lambda_1-\lambda_2)^2}}(e^{-\lambda_1 x} - e^{-\lambda_2 x}), \tag{E4c}$$

$$\lambda_{1,2} = \frac{1}{\sqrt{B_-B_+}}\left(\frac{|\bar{A}|}{2} \pm \sqrt{Z_{k_y}}\right), \tag{E4d}$$

$$Z_{k_y} = \left(\frac{\bar{A}^2}{4} - \frac{M}{B}B_+B_-\right) + \frac{D\bar{A}\sqrt{B_+B_-}}{B}k_y + B_+B_-k_y^2. \tag{E4e}$$

We have also defined:

$$\alpha_{k_y} = \tilde{R}_0\frac{B-D}{2Bk_y}\int_0^\infty f^*(x, k_y)[\partial_x + k_y]f(x, -k_y)$$
$$= \tilde{R}_0\frac{B-D}{2Bk_y}h(k_y)[\nu(k_y) + \xi(k_y)], \tag{E5a}$$

with

$$h(k_y) = 2\prod_{\pm}\sqrt{\frac{2\lambda_1^{\pm}\lambda_2^{\pm}(\lambda_1^{\pm}+\lambda_2^{\pm})}{(\lambda_1^{\pm}-\lambda_2^{\pm})^2}}, \tag{E6a}$$

$$\nu(k_y) = \lambda_1^{-}\left(\frac{1}{\lambda_1^{-}+\lambda_2^{+}} - \frac{1}{\lambda_1^{-}+\lambda_1^{+}}\right) + \lambda_2^{-}\left(\frac{1}{\lambda_1^{+}+\lambda_2^{-}} - \frac{1}{\lambda_2^{-}+\lambda_2^{+}}\right), \tag{E6b}$$

$$\xi(k_y) = \sum_{1,2}\frac{1}{\lambda_i^{-}+\lambda_i^{+}} - \sum_{\pm}\frac{1}{\lambda_1^{\pm}+\lambda_2^{\mp}}. \tag{E6c}$$

We have used the shorthand $\lambda_i^{\pm} = \lambda_i(\pm k_y)$.

[1] S. Groves and W. Paul, Phys. Rev. Lett. **11**, 194 (1963).
[2] S. Küfner and F. Bechstedt, Phys. Rev. B **91**, 035311 (2015).
[3] B. L. Booth and A. W. Ewald, Phys. Rev. **168**, 805 (1968).
[4] S. H. Groves, C. R. Pidgeon, A. W. Ewald, and R. J. Wagner, J. Phys. Chem. Solids **31**, 2031 (1970).
[5] B. J. Roman and A. W. Ewald, Phys. Rev. B **5**, 3914 (1972).
[6] A. A. Abrikosov and S. D. Beneslavksii, Zh. Eksp. Teor. Fiz. **59**, 1280 (1971) [Sov. Phys. JETP **32**, 669 (1971)].
[7] L. Fu and C. L. Kane, Phys. Rev. B **76**, 045302 (2007).
[8] H. Huang and F. Liu, Phys. Rev. B **95**, 201101 (2017).
[9] M. R. Scholz, V. A. Rogalev, L. Dudy, F. Reis, F. Adler, J. Aulbach, L. J. Collins-McIntyre, L. B. Duffy, H. F. Yang, Y. L. Chen, T. Hesjedal, Z. K. Liu, M. Hoesch, S. Muff, J. H. Dil, J. Schäfer, and R. Claessen, Phys. Rev. B **97**, 075101 (2018).
[10] Y. Ohtsubo, P. Le Fèvre, F. Bertran, and A. Taleb-Ibrahimi, Phys. Rev. Lett. **111**, 216401 (2013).
[11] V. A. Rogalev, T. Rauch, M. R. Scholz, F. Reis, L. Dudy, A. Fleszar, M.-A. Husanu, V. N. Strocov, J. Henk, I. Mertig, J. Schäfer, and R. Claessen, Phys. Rev. B **95**, 161117 (2017).
[12] A. Barfuss, L. Dudy, M. R. Scholz, H. Roth, P. Höpfner, C. Blumenstein, G. Landolt, J. H. Dil, N. C. Plumb, M. Radovic, A. Bostwick, E. Rotenberg, A. Fleszar, G. Bihlmayer, D. Wortmann, G. Li, W. Hanke, R. Claessen, and J. Schäfer, Phys. Rev. Lett. **111**, 157205 (2013).
[13] J.-C. Rojas-Sánchez, S. Oyarzún, Y. Fu, A. Marty, C. Vergnaud, S. Gambarelli, L. Vila, M. Jamet, Y. Ohtsubo, A. Taleb-Ibrahimi, P. Le Fèvre, F. Bertran, N. Reyren, J.-M. George, and A. Fert, Phys. Rev. Lett. **116**, 096602 (2016).
[14] C.-Z. Xu, Y.-H. Chan, Y. Chen, P. Chen, X. Wang, C. Dejoie, M.-H. Wong, J. A. Hlevyack, H. Ryu, H.-Y. Kee, N. Tamura, M.-Y. Chou, Z. Hussain, S.-K. Mo, and T.-C. Chiang, Phys. Rev. Lett. **118**, 146402 (2017).
[15] C.-Z. Xu, Y.-H. Chan, P. Chen, X. Wang, D. Flötotto, J. A. Hlevyack, G. Bian, S.-K. Mo, M.-Y. Chou, and T.-C. Chiang, Phys. Rev. B **97**, 035122 (2018).
[16] S. Takatani and Y. W. Chung, Phys. Rev. B **31**, 2290 (1985).
[17] Y. Zhang, K. He, C.-Z. Chang, C.-L. Song, L.-L. Wang, X. Chen, J.-F. Jia, Z. Fang, X. Dai, W.-Y. Shan, S.-Q. Shen, Q. Niu, X.-L. Qi, S.-C. Zhang, X.-C. Ma, and Q.-K. Xue, Nature Phys. **6**, 584 (2010).
[18] M. G. Burt, Semicond. Sci. Technol. **3**, 739 (1988).
[19] S. Küfner, M. Fitzner, and F. Bechstedt, Phys. Rev. B **90**, 125312 (2014).
[20] S. Küfner, J. Furthmüller, L. Matthes, and F. Bechstedt, Nanotechnol. **24**, 405702 (2013).
[21] S. Küfner and F. Bechstedt, Phys. Rev. B **89**, 195312 (2014).
[22] S. Küfner, L. Matthes, and F. Bechstedt, Phys. Rev. B **93**, 045304 (2016).
[23] B. A. Bernevig, T. L. Hughes, and S.-C. Zhang, Science **314**, 1757 (2006).
[24] M. König, S. Wiedmann, C. Brüne, A. Roth, H. Buhmann, L. W. Molenkamp, X.-l. Qi, and S.-c. Zhang, Science **318**, 766 (2007).
[25] D. G. Rothe, R. W. Reinthaler, C.-X. Liu, L. W. Molenkamp, S.-C. Zhang, and E. M. Hankiewicz, New J. Phys. **12**, 065012 (2010).
[26] E. O. Kane, J. Phys. Chem. Solids **1**, 249 (1957).
[27] J. Los, A. Fasolino, and A. Catellani, Phys. Rev. B **53**, 4630 (1996).
[28] B. A. Foreman, Phys. Rev. B **48**, 4964 (1993).
[29] B. A. Foreman, Phys. Rev. B **56**, R12748 (1997).
[30] R. Winkler, *Spin-orbit Coupling Effects in Two-Dimensional Electron and Hole Systems*, Springer Tracts in Modern Physics (Springer, Berlin, 2003).
[31] L. C. L. Y. Voon and M. Willatzen, *The k p Method: Electronic Properties of Semiconductors* (Springer, Berlin, 2009).
[32] E. G. Novik, A. Pfeuffer-Jeschke, T. Jungwirth, V. Latussek, C. R. Becker, G. Landwehr, H. Buhmann, and L. W. Molenkamp, Phys. Rev. B **72**, 035321 (2005).
[33] T. Brudevoll, D. S. Citrin, M. Cardona, and N. E. Christensen, Phys. Rev. B **48**, 8629 (1993).
[34] D. Price and J. Rowe, Solid State Commun. **7**, 1433 (1969).
[35] S. Adachi, *Properties of Group-IV, III-V and II-VI Semiconductors* (Wiley, New York, 2005).
[36] G. E. Pikus and G. L. Bir, Fiz. Tverd. Tela (Leningrad) **1**, 1642 (1959) [Sov. Phys. - Solid State **1**, 1502 (1960)].
[37] T. B. Bahder, Phys. Rev. B **41**, 11992 (1990).
[38] M. G. Burt, J. Phys.: Condens. Matter **4**, 6651 (1992).
[39] O. E. Raichev, Phys. Rev. B **85**, 045310 (2012).
[40] H.-Z. Lu, W.-Y. Shan, W. Yao, Q. Niu, and S.-Q. Shen, Phys. Rev. B **81**, 115407 (2010).
[41] C. Brüne, C. X. Liu, E. G. Novik, E. M. Hankiewicz, H. Buhmann, Y. L. Chen, X. L. Qi, Z. X. Shen, S. C. Zhang, and L. W. Molenkamp, Phys. Rev. Lett. **106**, 126803 (2011).
[42] M. M. Asmar, D. E. Sheehy, and I. Vekhter, Phys. Rev. B **97**, 075419 (2018).

[43] L. Ortiz, R. A. Molina, G. Platero, and A. M. Lunde, Phys. Rev. B **93**, 205431 (2016).

[44] M. Franz and L. Molenkamp, *Topological Insulators* (Elsevier, Amsterdam, 2013).

[45] T. Schumann, L. Galletti, D. A. Kealhofer, H. Kim, M. Goyal, and S. Stemmer, Phys. Rev. Lett. **120**, 016801 (2018).

[46] P. Folkes, P. Taylor, C. Rong, B. Nichols, H. Hier, T. Gao, N. P. Ong, O. Vail, and G. de Coster (unpublished).

[47] R. Farrow, D. Robertson, G. Williams, A. Cullis, G. Jones, I. Young, and P. Dennis, J. Cryst. Growth **54**, 507 (1981).